

## A Appendix

### A.1 Algorithm

The algorithm for the proposed framework is described in algorithm 1. First, the target design objective  $\phi$  and the set of equality constraints  $h_j$  are specified along with an initial topology. Note that defining an initial topology is equivalent to initializing the neural network (NN). Thus the NN is initialized such that the density output matches the desired initial topology. Next, the domain is discretized into finite elements and the element centers serve as input to the neural network, which returns the elemental densities  $\rho$  as discussed in section 3.2. Homogenization is performed which predicts the homogenized structural response from the elemental densities as per section 2.1. Based on the results from homogenization, the objective  $\phi$  eq. (7a) and the constraints  $h_j$  eq. (7c) are evaluated. Next, the loss function  $L$  is computed using eq. (10), and the gradient of the loss function with respect to the neural network weights ( $\nabla L$ ) is computed through automatic differentiation. The NN is then trained using PyTorch’s L-BFGS optimizer as described in section 3.3, which requires the update of Lagrangian parameters  $\alpha, \mu$ . The training procedure continues until the convergence criteria are met. The globally-defined activation functions, used in representing the density field, provide for implicit filtering. This is analogous to implicit filtering supported by the B-spline representation of the density field [28].

---

#### Algorithm 1 Microstructural TO using NN

---

<pre> 1: <b>procedure</b> MICROTOUNN(<math>\Omega_0, \phi, \dots</math>) 2:   <math>\Omega^{init} \rightarrow \mathbf{w}</math> 3:   <math>\Omega^0 \rightarrow \Omega_h^0</math> 4:   <math>\mathbf{x} = \{x_e, y_e\}_{e \in \Omega_h^0}</math> 5:   <math>k = 0; \alpha_i = \alpha_0; \mu_i = 0 \forall i</math> 6:   <b>repeat</b> 7:     <math>NN(\mathbf{x}; \mathbf{w}) \rightarrow \rho</math> 8:     <math>\rho \rightarrow \mathbf{C}^H</math> 9:     <math>\mathbf{C}^H \rightarrow \phi</math> 10:    <math>\{\mathbf{C}^H, \rho\} \rightarrow h_j</math> 11:    <math>\{\phi, h, \alpha_i, \mu_i\} \rightarrow L</math> 12:    <math>AD(L \leftarrow \mathbf{w}) \rightarrow \nabla L</math> 13:    <math>\mathbf{w} + \Delta \mathbf{w}(\nabla L) \rightarrow \mathbf{w}</math> 14:    <math>k++</math> 15:    Update <math>\alpha_i, \mu_i</math> 16:  <b>until</b> <math>\Delta \phi &lt; \hat{\epsilon}_\phi</math> and <math>\Delta h &lt; \hat{\epsilon}_h</math> and <math>k &lt; k_{max}</math> 17:  <b>return</b> <math>\mathbf{w}</math> 18: <b>end procedure</b> </pre>	<pre> ▷ Inputs ▷ Initialize NN weights ▷ Domain discretization ▷ elem centers; NN input ▷ Initialization (section 3.3) ▷ Optimization (Training) ▷ Fwd prop NN ▷ Homogenization (section 2.1) ▷ Compute design objective eq. (7a) ▷ Compute constraints eq. (7c) ▷ Loss from Equation (10) ▷ Auto diff for sensitivity ▷ L-BFGS step ▷ Aug-Lag terms eq. (11a), eq. (11b) ▷ convg. criteria </pre>
--	--

---

### A.2 Impact of Initial Topology

Next, we consider initial designs different from Figure 7 and study their impact on the optimal topology, with all other parameters are kept constant at default values. Specifically, we revisit the problem of maximizing the bulk modulus, subject to a mass-fraction constraint of 0.3.

For the initial topology of a circular hole in Figure 14a, the final topology is illustrated in Figure 14b. Similarly, with the initial topology of four circular holes in Figure 15a, the final topology, for the same problem is illustrated in Figure 15b, with  $K^* = 0.089$ .

Although the designs are different, the final bulk moduli are comparable. Thus, one can potentially discover different designs by changing the initial design.

### A.3 Impact of NN Size

We now vary the neural-network size and minimize the Poisson ratio, subject to a mass-fraction constraint of 0.3 (with default parameters). Figure 16 illustrates various designs obtained for different NN configurations. The final Poisson ratio  $\nu^*$  for the three cases are -0.60, -0.57 and -0.82 respectively.

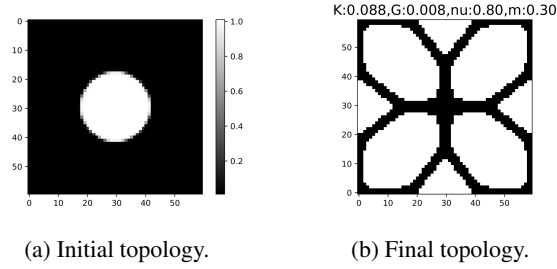


Figure 14: Maximizing bulk modulus with mass constraint.

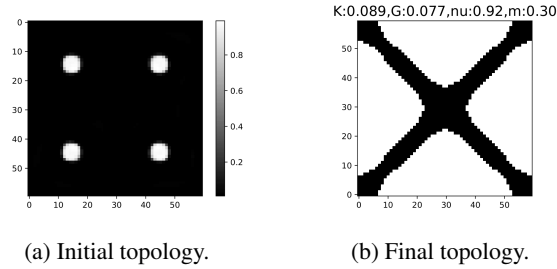


Figure 15: Maximizing bulk modulus with mass constraint.

The number of design variables are 272, 1782 and 18,602 respectively. We observe that as the number of design variables is increased, the algorithm tends to generate more complex designs. But, we did not observe any pattern between the NN size and the final objective achieved. One can however observe single-node connections in some of the designs; this has been observed in NPR designs by other researchers as well [30]; dilation methods such as the ones proposed in[2] need to be explored to address this issue.

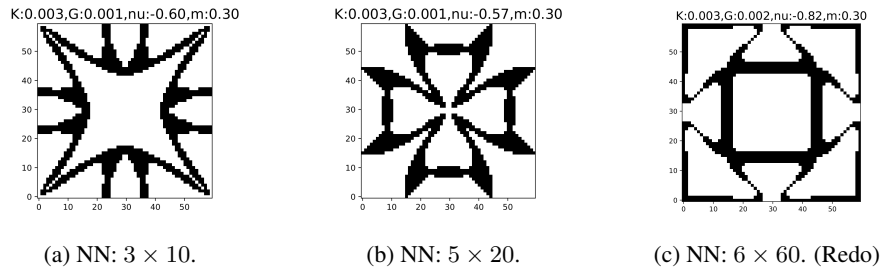


Figure 16: Minimizing Poisson ratio with mass constraint using different NNs.

#### A.4 Impact of Mesh Size

Next, we vary the mesh size and minimize the Poisson ratio, subject to a mass constraint of 0.3 (with all other parameters at default). Figure 17 illustrates the designs obtained for different mesh sizes. The final Poisson ratio  $\nu^*$  for the three cases are -0.57, -0.60 and -0.86 respectively. We observe that the topology is sensitive to the mesh discretization; this is usually not desirable in topology optimization [33]. Further investigation is needed to study the interplay between the neural network and mesh discretization.

#### A.5 Sampling at Higher Resolution

Once the optimization is completed, the global representation of the density field via the NN allows us to sample the field at a finer resolution and extract a high-resolution topology at no additional cost.

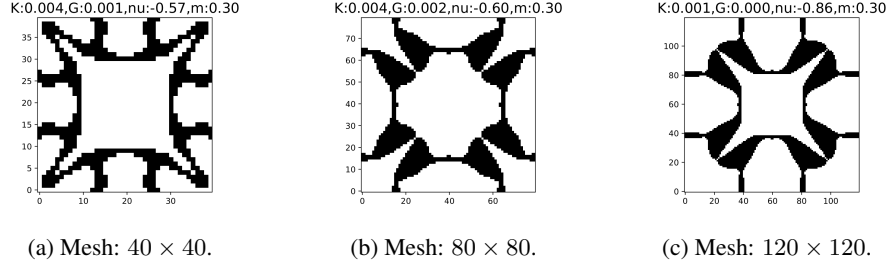


Figure 17: Minimizing Poisson ratio for different mesh sizes.

This is illustrated in Figures 18 and 19. Observe that we exploit the non-linear NN representation of the density field for resampling, i.e., it is not a simple linear interpolation between pixels. In other words, suppose  $d_1 = NN(x_1, y_1)$  and  $d_2 = NN(x_2, y_2)$  are the density values at two neighboring pixels. A linear interpolation will yield  $0.5(d_1 + d_2)$ , whereas the non-linear interpolation yields  $NN(0.5(x_1 + x_2), 0.5(y_1 + y_2))$ .

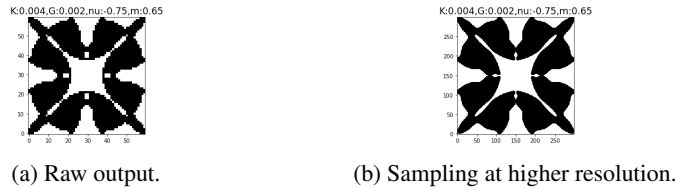


Figure 18: Sampling the neural network at a higher resolution.

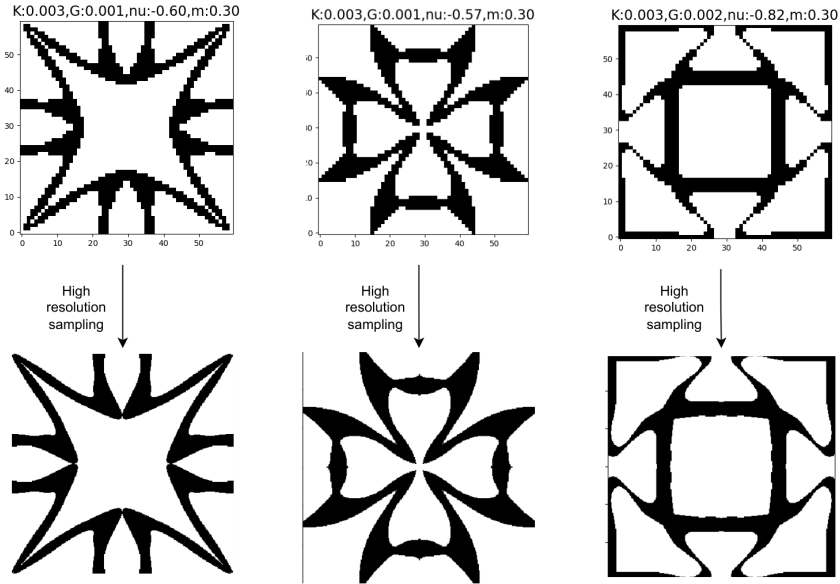


Figure 19: Results of Figure 16 are sampled at  $5\times$  resolution ( $60 \times 60 \rightarrow 300 \times 300$ )

## A.6 Evaluation of Poisson Ratio

We consider the negative Poisson's ratio microstructures generated in appendix A.3 and evaluate them using ANSYS [25]. Specifically, the output topology is sampled at a high resolution (in this case 5 times, as seen in Figure 19) and converted to a 2D part using SolidWorks. This is then imported into ANSYS Workbench, where a small axial strain is prescribed and the resultant transverse strain is

measured to compute the Poisson’s ratio. The results are tabulated in table 3. One can observe that the topology with no single-node connection (fig. 16b) is in good agreement with the results from ANSYS. However, we note that the other two topologies have single-node/hinge connections and, not surprisingly, the homogenized values differ significantly from ANSYS results. Eliminating the single-node/hinge connections is important both for manufacturability and for accurate modeling; this will be explored in the future using, for example, methods described in [23, 42].

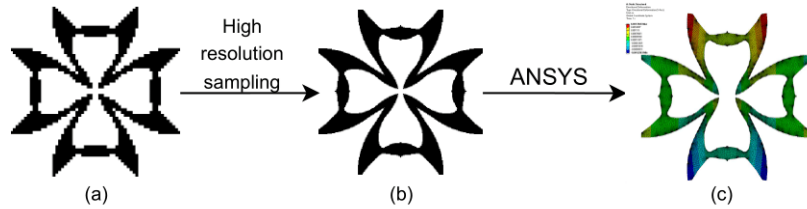


Figure 20: (a) Topology using the default mesh. (b) topology sampled at high resolution. (c) High-resolution geometry imported and analyzed using ANSYS.

Topology	Homogenized (coarse)	Homogenized (resampled)	ANSYS
fig. 16a	-0.60	-0.65	-1.00
fig. 16b	-0.57	-0.57	-0.60
fig. 16c	-0.82	-0.87	-1.12

Table 3: Evaluation of Poisson’s ratio.

### A.7 Multiple Materials

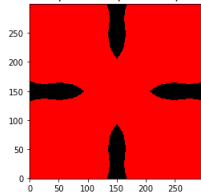
Next consider maximization of  $K$ , subject to a mass constraint ( $\hat{m} = 0.3$ ), with two, three and four materials. The material properties are summarized in Table 4.

Material	Color code	$E$	$\nu$	$\lambda$
0	White	0.001	0.3	0
1	Black	1	0.3	1
2	Red	0.2	0.3	0.2
3	Green	0.3	0.3	0.25
4	Blue	0.4	0.3	0.3

Table 4: Material properties.

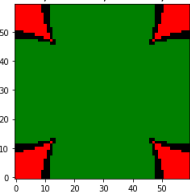
The results are illustrated in Figure 21 (compare against Figure 8a for single material). The final bulk modulus  $K^*$  for the three cases are 0.172, 0.225 and 0.240, respectively (compared to 0.091 for single material). Observe that the bulk modulus increases as additional materials are introduced.

K:0.172,G:0.089,nu:0.29,m:0.30



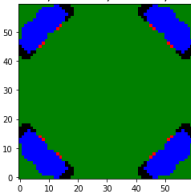
(a) Two materials.

K:0.225,G:0.119,nu:0.29,m:0.30



(b) Three materials.

K:0.240,G:0.129,nu:0.30,m:0.30



(c) Four materials.

Figure 21: Maximizing  $K$  with mass constraint using multiple materials.